Available online at www.sciencedirect.com
SCIENCE DIRECT®
ELSEVIER
International Journal of Solids and Structures 42 (2005) 6277–6298
INTERNATIONAL JOURNAL OF SOLIDS and STRUCTURES
www.elsevier.com/locate/ijsolstr

# A computational study of local stress intensity factor solutions for kinked cracks near spot welds in lap-shear specimens

D.-A. Wang [a], J. Pan [b,*]

[a] *Institute of Precision Engineering, National Chung Hsing University, Taichung 402, Taiwan*
[b] *Mechanical Engineering, The University of Michigan, 2250 GGB Building, Ann Arbor, MI 48109-2125, USA*

Received 22 June 2004; received in revised form 26 May 2005
Available online 20 July 2005

**Abstract**

In this paper, the local stress intensity factor solutions for kinked cracks near spot welds in lap-shear specimens are investigated by finite element analyses. Based on the experimental observations of kinked crack growth mechanisms in lap-shear specimens under cyclic loading conditions, three-dimensional and two-dimensional plane-strain finite element models are established to investigate the local stress intensity factor solutions for kinked cracks emanating from the main crack. Semi-elliptical cracks with various kink depths are assumed in the three-dimensional finite element analysis. The local stress intensity factor solutions at the critical locations or at the maximum depths of the kinked cracks are obtained. The computational local stress intensity factor solutions at the critical locations of the kinked cracks of finite depths are expressed in terms of those for vanishing kink depth based on the global stress intensity factor solutions and the analytical kinked crack solutions for vanishing kink depth. The three-dimensional finite element computational results show that the critical local mode I stress intensity factor solution increases and then decreases as the kink depth increases. When the kink depth approaches to 0, the critical local mode I stress intensity factor solution appears to approach to that for vanishing kink depth based on the global stress intensity factor solutions and the analytical kinked crack solutions for vanishing kink depth. The two-dimensional plane-strain computational results indicate that the critical local mode I stress intensity factor solution increases monotonically and increases substantially more than that based on the three-dimensional computational results as the kink depth increases. The local stress intensity factor solutions of the kinked cracks of finite depths are also presented in terms of those for vanishing kink depth based on the global stress intensity factor solutions and the analytical kinked crack solutions for vanishing kink depth. Finally, the implications of the local stress intensity factor solutions for kinked cracks on fatigue life prediction are discussed.


* Corresponding author. Tel.: +1 734 764 9404; fax: +1 734 647 3170.
*E-mail address:* jwo@umich.edu (J. Pan).

0020-7683/$ - see front matter © 2005 Elsevier Ltd. All rights reserved.
doi:10.1016/j.ijsolstr.2005.05.036

*Keywords:* Spot weld; Stress intensity factor; Kinked crack; Mixed mode; Fracture; Fatigue

## 1. Introduction

Resistance spot welding is widely used to join sheet metals for automotive components. The fatigue lives of spot welds have been investigated by many researchers in various types of specimens, for example, see Zhang (1999). Since the spot weld provides a natural crack or notch along the weld nugget circumference, fracture mechanics has been adopted to investigate the fatigue lives of spot welds in various types of specimens based on the stress intensity factor solutions at the critical locations of spot welds (Pook, 1975, 1979; Radaj and Zhang, 1991a,b, 1992; Swellam et al., 1994; Zhang, 1997, 1999, 2001).

As discussed in Swellam et al. (1992), the spot weld fatigue failure process can be divided into three stages in lap-shear specimens. Stage I corresponds to the crack initiation and growth as kinked cracks emanating from the critical locations of the main crack along the nugget circumference up to about 18% of the sheet thickness. Stage II corresponds to the crack propagation through the sheet thickness. Stage III corresponds to the crack propagation through the width of specimens. Note that the fatigue life of a spot weld is in general dominated by stages I and II of fatigue failure process. Therefore, accurate stress intensity factor solutions for kinked cracks emanating from the critical locations of the main crack along the circumference of spot welds through the sheet thickness are needed to estimate the fatigue life based on the linear elastic fracture mechanics.

First, the global stress intensity factors for a main crack and the local stress intensity factors for a kinked crack are defined here. Fig. 1 shows a schematic plot of a main crack and a kinked crack with the kink depth $d$ and the kink angle $\alpha$. Without the kinked crack ($d = 0$), $K_{\mathrm{I}}$, $K_{\mathrm{II}}$ and $K_{\mathrm{III}}$ represent the global mode I, II and III stress intensity factors for the main crack, respectively. With the kinked crack ($d \neq 0$), $k_{\mathrm{I}}$, $k_{\mathrm{II}}$ and $k_{\mathrm{III}}$ represent the local mode I, II and III stress intensity factors for the kinked crack, respectively. Note that the arrows in the figure schematically represent the positive global and local stress intensity factors $K_{\mathrm{I}}$, $K_{\mathrm{II}}$, $K_{\mathrm{III}}$, $k_{\mathrm{I}}$, $k_{\mathrm{II}}$ and $k_{\mathrm{III}}$. For kinked cracks, when the kink depth $d$ approaches to 0, the in-plane local stress intensity factors $k_{\mathrm{I}}$ and $k_{\mathrm{II}}$ can be expressed as closed-form functions of the kink angle $\alpha$ and the global $K_{\mathrm{I}}$ and $K_{\mathrm{II}}$ for the main crack (Bilby et al., 1978; Cotterell and Rice, 1980). The closed-form kinked crack solutions will be used as the basis to present our numerical stress intensity factor solutions in this investigation in contrast to those of Pan and Sheppard (2003).

In order to obtain accurate stress and strain distributions and/or stress intensity factor solutions for spot welds in lap-shear specimens, three-dimensional finite element analyses have been carried out by various investigators (Radaj et al., 1990; Satoh et al., 1991; Deng et al., 2000; Pan and Sheppard, 2002, 2003). Radaj

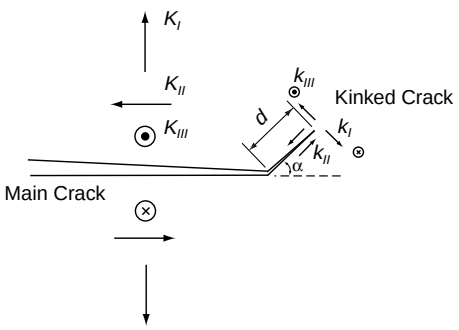


Fig. 1. A schematic plot of a main crack and a kinked crack with the kink depth $d$ and the kink angle $\alpha$.

et al. (1990) used a finite element model where plate and brick elements are used for sheets and spot welds, respectively, to obtain the global stress intensity factor solutions along the nugget circumference for the main cracks in various specimens. Satoh et al. (1991) conducted three-dimensional elastic and elastic–plastic finite element analyses to investigate the stress and strain distributions in the symmetry plane near spot welds in lap-shear specimens to identify the fatigue crack initiation sites under high-cycle and low-cycle fatigue loading conditions. Deng et al. (2000) conducted elastic and elastic–plastic three-dimensional finite element analyses to investigate the stress fields near the nuggets in lap-shear and symmetrical coach peel specimens to understand the effects of the nugget size and the thickness on the interface and nugget pull out failure modes. Pan and Sheppard (2002) also used a three-dimensional elastic–plastic finite element analysis to correlate the fatigue lives to the cyclic plastic strain ranges for the material elements near the main notch in lap-shear specimens and modified coach-peel specimens. Pan and Sheppard (2003) conducted a three-dimensional finite element analysis to investigate the critical local stress intensity factor solutions for semi-elliptical kinked cracks emanating from the main crack along the nugget circumference in lap-shear specimens and modified coach-peel specimens.

Recently, Lin and Pan (2004) and Lin et al. (in press) took the two-dimensional kinked crack approach of Newman and Dowling (1998) to investigate the fatigue lives of spot welds in various types of specimens of dual phase steel, low carbon steel and high strength steel. The fatigue life predictions based on the global stress intensity factor solutions and the closed-form kinked crack solutions agree well with the experimental results. Note that the closed-form local stress intensity factor solutions for kinked cracks used in Newman and Dowling (1998), Lin and Pan (2004) and Lin et al. (in press) are supposedly for kinked cracks with a vanishing kink depth. The fatigue models in Newman and Dowling (1998), Lin and Pan (2004) and Lin et al. (in press) are based on the assumption that the local stress intensity factor solutions remain relatively constant as kinked cracks grow through the thickness in their two-dimensional crack growth models. It is necessary to understand the dependence of the local stress intensity factor solutions on the kink depth at the critical locations of spot welds in lap-shear specimens in order to validate the engineering fatigue models in Newman and Dowling (1998), Lin and Pan (2004) and Lin et al. (in press). For lap-shear type specimens, the global stress intensity factors vary from point to point. The kinked crack geometry observed in experiments is curved and three-dimensional. The critical local stress intensity factor solutions for three-dimensional kinked cracks in lap-shear type specimens have been obtained by Pan and Sheppard (2003) by three-dimensional finite element analyses. Their local stress intensity factor solutions for semi-elliptical kinked cracks are expressed in terms of the mode I stress intensity factor solutions for semi-elliptical surface cracks of Newman and Raju (1981) for their specific geometries of specimens.

Fig. 2(a) and (b) schematically shows a lap-shear specimen and a square-cup specimen, respectively, used to investigate the strength and fatigue lives of spot welds. For clear demonstration of spot weld locations, only halves of the specimens are shown. The spot welds are idealized as circular cylinders and shown as shaded half cylinders in the figures. The half lap-shear specimen with the thickness $t$, the width $W$, the nugget radius $b$, the overlap length $V$ of the upper and lower sheets, and the length $L$ is shown in Fig. 2(a). Lap-shear specimens are often used to investigate the behavior of spot welds under shear dominant loading conditions. Note that two spacers of the length $S$ are attached to the both ends of the lap-shear specimen in order to induce a pure shear to the interfacial plane of the nugget for the two sheets and to avoid the initial realignment of the specimen during testing. The square-cup specimen with the thickness $t$ and the width $E$ is shown in Fig. 2(b). For the given geometry of the square-cup specimen, the nugget has a nearly uniform loading condition and nearly uniform stress intensity factor solutions along the nugget circumference when the ratio of the width $E$ to the nugget diameter is large and the specimen is under pure opening loading conditions (Wang et al., 2005). The details on the design of square-cup specimens were discussed in Wung and Stewart (2001).

Axisymmetric finite element analyses were used to investigate the local stress intensity factor solutions at the kinked crack tip in cup specimens (Wang et al., 2005). The computational results indicate that when the

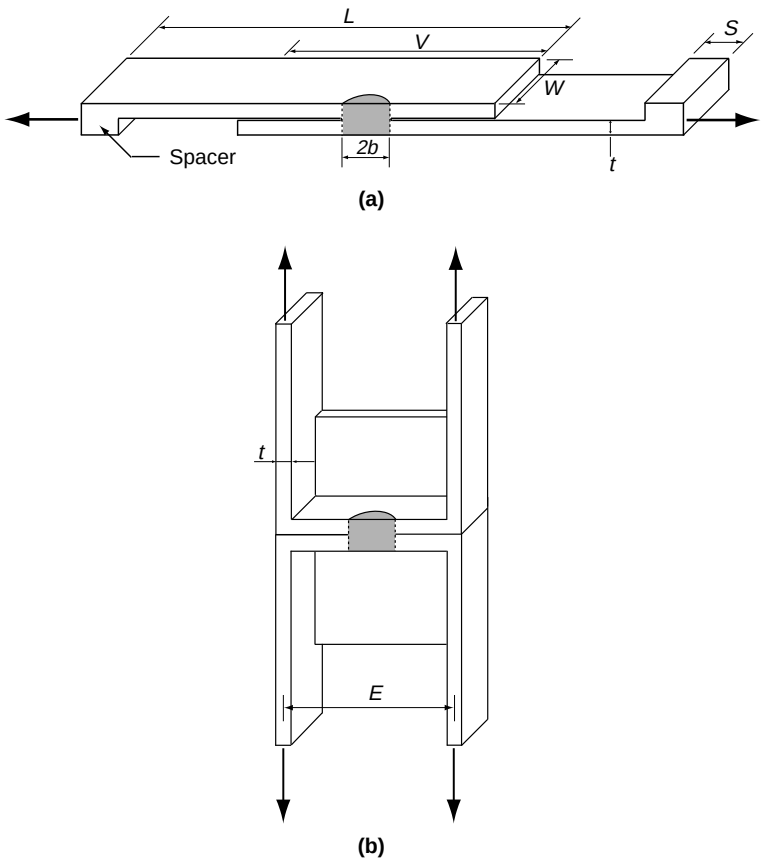


Fig. 2. Schematic plots of two types of spot weld specimens are shown. (a) A half lap-shear specimen under the applied force (shown as the bold arrows). (b) A half square-cup specimen under the applied force (shown as the bold arrows).

kink depth decreases, the local mode I stress intensity factor solution for a sharp main crack and a circular main notch approaches to that based on the closed-form solution for a kinked crack with a vanishing kink depth and a kink angle of 90°. The computational results also indicate that when the kink depth increases, the local mode I stress intensity factor solution increases substantially. This trend is quite different from that based on the three-dimensional finite element analysis by Pan and Sheppard (2003) for lap-shear type specimens. Therefore, an investigation of the local stress intensity factor solutions for kinked cracks in lap-shear specimens is conducted and the results are reported here. Based on the work of Wang et al. (2005) as mentioned earlier, the computational results are presented in a normalized form with respect to the closed-form solution for kinked cracks with a vanishing kink depth in this investigation, in contrast to those presented in Pan and Sheppard (2003) based on the surface crack solution of Newman and Raju (1981).

In this paper, a three-dimensional finite element model based on the finite element model for two circular plates with connection (Wang et al., 2005) is first used to obtain the global stress intensity factor solutions along the nugget circumference for the lap-shear specimens of Lin et al. (in press). The distributions of the local stress intensity factor solutions for kinked cracks with a vanishing kink depth along the nugget circumference are then obtained from the global stress intensity factor solutions and the analytical kinked crack solutions for vanishing kink depth. Next, based on the experimental observations of the kinked crack growth mechanisms in lap-shear specimens under cyclic loading conditions in Lin and Pan (2004) and Lin

et al. (in press), three-dimensional finite element models for kinked cracks emanating from the critical locations of the main crack are established to investigate the local stress intensity factor solutions. Semi-elliptical kinked cracks emanating from the critical locations of the main crack along the nugget circumference and various kink depths are considered. The local stress intensity factor solutions at the critical locations or at the maximum depths of the kinked cracks are obtained. A two-dimensional plane-strain finite element model for kinked cracks is also established to investigate the local stress intensity factor solutions and to examine the applicability of using a two-dimensional kinked crack model to characterize the local stress intensity factor solutions at the critical locations of the semi-elliptical kinked cracks. The local stress intensity solutions for kinked cracks emanating from continuous lap joints are also presented under combined tension and bending conditions. Finally, the implications of the local stress intensity factor solutions for kinked cracks in lap-shear specimens for fatigue life prediction are discussed.

## 2. Local stress intensity factor solutions for kinked cracks

The fatigue cracking mechanisms of spot welds in different types of specimens are different due to different geometries and loading conditions. The kink paths in different types of specimens were discussed in Lin and Pan (2004) and Lin et al. (in press). Fig. 3(a) shows a schematic plot of the symmetry cross-section of a lap-shear specimen with the sheet thickness $t$ under the applied force $P$. Fig. 3(b) shows a micrograph of the symmetry cross-section near a failed spot weld in a lap-shear specimen of dual phase steel sheet of 0.65 mm thickness (Lin et al., in press). The kinked crack appears to grow from the main notch or crack tip to the surface of the sheet. Fig. 3(c) shows a schematic plot of the symmetry cross-section near a spot

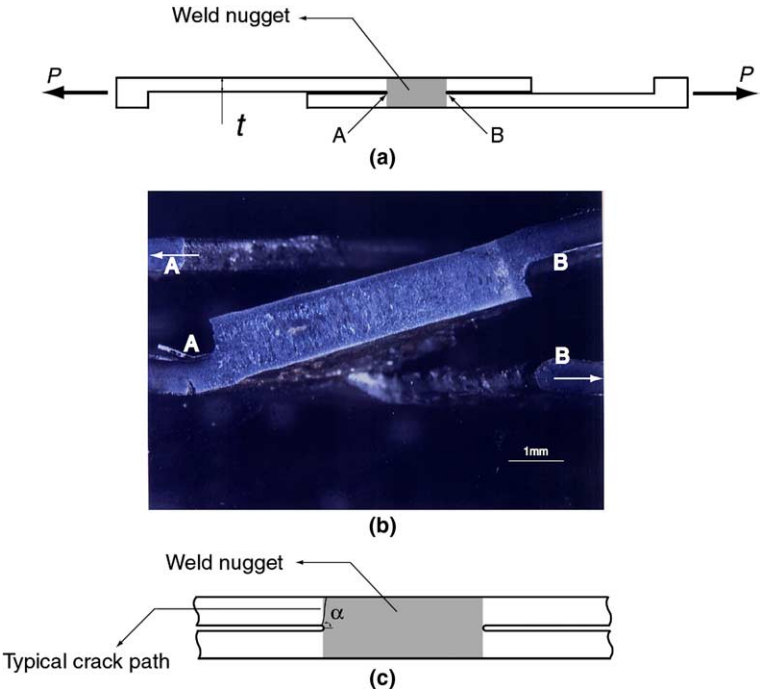


Fig. 3. (a) A schematic plot of the symmetry cross-section of a lap-shear specimen and the applied force $P$ shown as the bold arrows. (b) A micrograph of the symmetry cross-section of a failed spot weld in a lap-shear specimen of dual phase steel sheet under cyclic loading conditions. (c) A schematic plot of the symmetry cross-section near a spot weld.

weld. The fatigue crack can be idealized to grow from the main notch or crack tip with a kink angle $\alpha$ as shown in Fig. 3(c). The kink angle $\alpha$ appears to be near 90° for lap-shear specimens under cyclic loading conditions. Note that as shown in a parametric study in Lin and Pan (2004), when the selection of the kink angle is close to 90°, the fatigue life prediction will not be critically dependent upon the selection of the kink angle. The computational results for the critical local stress intensity factor solutions for semi-elliptical kinked cracks emanating from the main notch at different angles in Pan and Sheppard (2003) also suggest that the local stress intensity factor solutions do not depend critically on the kink angle.

Fig. 3(c) also schematically shows that a kinked crack emanating from the critical location (point A as shown in Fig. 3(a)). Note that due to symmetry, kinked cracks can emanate from either of the two critical locations (points A and B as shown in Fig. 3(a)). However, only one of them will become the dominant kinked crack and lead to the initial through-thickness failure of the spot weld in lap-shear specimens (Swellam et al., 1992). This is the reason that we concentrate on single kinked crack for lap-shear specimens in our computations here. Microscopically speaking, the main crack tips as observed from the sectional views of spot welds usually have finite root radii. The effects of the notch geometry on the local stress intensity factor solutions for kinked cracks have been studied in Wang et al. (2005). However, when the main crack is treated as a sharp crack, the global stress intensity factor solutions can be used to correlate the fatigue lives of spot welds, see Zhang (1999).

When the main crack is considered as a sharp crack and the kink depth approaches to 0, the in-plane local stress intensity factors $k_{\mathrm{I}}$ and $k_{\mathrm{II}}$ can be expressed as closed-form functions of the kink angle $\alpha$ and the global stress intensity factors $K_{\mathrm{I}}$ and $K_{\mathrm{II}}$ for the main crack. The local $k_{\mathrm{I}}$ and $k_{\mathrm{II}}$ solutions can be expressed as (Bilby et al., 1978; Cotterell and Rice, 1980)

$$k_{\mathrm{I}} = \frac{1}{4}\left(3\cos\frac{\alpha}{2} + \cos\frac{3\alpha}{2}\right)K_{\mathrm{I}} + \frac{3}{4}\left(\sin\frac{\alpha}{2} + \sin\frac{3\alpha}{2}\right)K_{\mathrm{II}} \tag{1}$$

$$k_{\mathrm{II}} = -\frac{1}{4}\left(\sin\frac{\alpha}{2} + \sin\frac{3\alpha}{2}\right)K_{\mathrm{I}} + \frac{1}{4}\left(\cos\frac{\alpha}{2} + 3\cos\frac{3\alpha}{2}\right)K_{\mathrm{II}} \tag{2}$$

For mode III loadings, without a rigorous proof as in Cotterell and Rice (1980) for in-plane mode, the local $k_{\mathrm{III}}$ solution can be expressed as

$$k_{\mathrm{III}} = \cos\frac{\alpha}{2}K_{\mathrm{III}} \tag{3}$$

It is noted that the kinked crack growth in lap-shear specimens is under local combined mode I, II and III loading conditions.

Note that Eqs. (1)–(3) are only appropriate when the kink depth approaches to 0. In order to predict the total fatigue lives of spot welds based on the linear elastic fracture mechanics, the local $k_{\mathrm{I}}$, $k_{\mathrm{II}}$ and $k_{\mathrm{III}}$ solutions are needed for both the infinitesimal and the finite kink depth in specimens. The local $k_{\mathrm{I}}$ and $k_{\mathrm{II}}$ solutions for kinked cracks with a finite kink depth were presented by Kitagawa et al. (1975) and Lo (1978). But the solutions presented by Kitagawa et al. (1975) and Lo (1978) are restricted to the problems of kinked cracks in a two-dimensional infinite solid under prescribed uniform tensile stress at infinity. For semi-elliptical kinked cracks in spot weld specimens with complex geometry and non-uniform remote stress state, numerical methods such as boundary element or finite element methods may be a convenient way to extract the local $k_{\mathrm{I}}$, $k_{\mathrm{II}}$ and $k_{\mathrm{III}}$ solutions.

The local stress intensity factor solutions for kinked cracks can be used to predict the fatigue lives of spot welds in various types of specimens based on the fatigue models of Newman and Dowling (1998), Lin and Pan (2004) and Lin et al. (in press). Past research on the stress intensity factors emphasizes the global stress intensity factors (Swellam et al., 1994; Zhang, 1997, 1999, 2001; Pan and Sheppard, 2003; Wang et al., in press). Based on the experimental observations on low carbon steel and high strength low alloy steel, Swellam et al. (1992) concluded that the stage I fatigue life corresponding to kinked crack initiation and

growth up to 18% of the sheet thickness constitutes more than 40% of the total fatigue life of the low carbon steel specimens for the life range of $10^5$–$10^7$ cycles as compared to stage II fatigue life for through-thickness crack propagation and stage III fatigue life for cross-width crack propagation in lap-shear specimens.

For shallow semi-elliptical kinked cracks emanating from the main crack in spot weld specimens, the local stress intensity factor solutions should be dominated by the distributions of the global stress intensity factor solutions near the shallow kinked cracks. Fig. 4(a) shows a schematic plot of a lap-shear specimen under the applied force $P$. As shown in Fig. 4(a), the critical locations with the maximum global mode I and II stress intensity factor solutions are marked as point A and point B, and the critical locations with the maximum global mode III stress intensity factor solution are marked as point C and point D. Fig. 4(b) shows a circular cylinder which represents the nugget in the lap-shear specimen. A semi-elliptical kinked crack with a kink angle $\alpha = 90°$ is shown to grow from the main crack. The kinked and main crack fronts are marked in the figure. Fig. 4(c) schematically shows the semi-elliptical kinked crack in the circumferential and depth directions. The location of point $P$ of the kinked crack front can be specified by that of the corresponding point $Q$ on the main crack front, which can then be characterized by the orientation angle $\theta$ as defined in Fig. 4(b). As shown in Fig. 4(c), point $E$ represents the location of the maximum kink depth. The maximum kink depth is denoted as $d$ and the half kinked crack length is denoted as $c$. As shown in Wang et al. (2005), the local stress intensity factor solutions approach to those based on the global stress

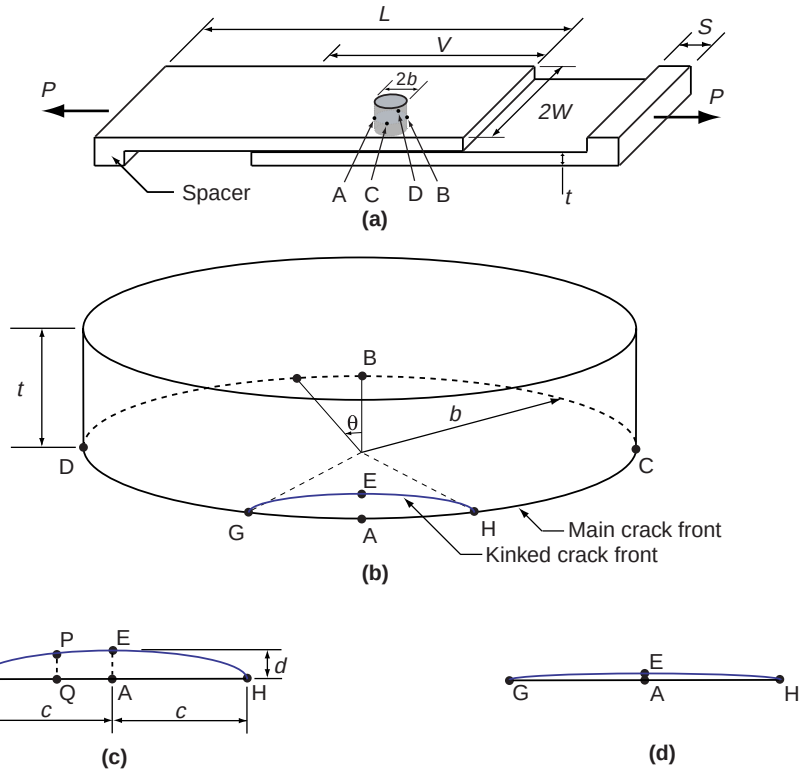


Fig. 4. (a) A schematic plot of a lap-shear specimen and the applied force $P$ shown as the bold arrows. The weld nugget is idealized as a circular cylinder and shown as a shaded cylinder. The critical locations with the maximum mode I and II stress intensity factor solutions are marked as points A and B. The critical locations with the maximum mode III stress intensity factor solution are marked as points C and D. (b) A circular cylinder represents a nugget of the specimen in the lap-shear specimen. A semi-elliptical kinked crack is also shown. (c) A schematic plot of the semi-elliptical kinked crack in the circumferential and depth directions. (d) A schematic plot of a shallow semi-elliptical kinked crack just initiated from the main crack.

intensity factor solutions and the analytical kinked crack solutions in Eqs. (1) and (2) with the kink angle $\alpha = 90°$ under axisymmetric loading conditions as the kink depth decreases for sharp main cracks in cup specimens. Therefore, as the normalized maximum kink depth $d/t$ decreases (as shown in Fig. 4(d)), the local stress intensity factor solutions should approach to those for vanishing kink depth based on the global stress intensity factor solutions and the analytical kinked crack solutions in Eqs. (1)–(3).

The local stress intensity factor solutions along the kinked crack front should be functions of the circumferential location denoted by $\theta$ (as defined in Fig. 4(b)). However, when $d/t$, $d/c$ and $c/b$ change, the local stress intensity factor solutions should also change. Therefore, the local stress intensity factor solutions at point $P$ as shown in Fig. 4(c) can be expressed as

$$k_i = k_i(\theta, d/t, d/c, c/b, K_{\mathrm{I}}, K_{\mathrm{II}}, K_{\mathrm{III}}), \quad i = \mathrm{I}, \mathrm{II}, \mathrm{III} \tag{4}$$

Here, the local stress intensity factor $k_i$ solutions are functions of the orientation angle $\theta$, the normalized maximum kink depth $d/t$, the aspect ratio $d/c$ of the semi-elliptical kinked crack, the normalized kinked crack length or the angle span of the kinked crack $c/b$, and the entire distributions of the global stress intensity factors $K_{\mathrm{I}}$, $K_{\mathrm{II}}$ and $K_{\mathrm{III}}$. Note that the entire distributions of the global $K_i$ along the nugget circumference can influence the local $k_i$ solutions at $\theta$ for a given set of $d/t$, $d/c$ and $c/b$. However, the global $K_i$ solutions close to the kinked crack front should have dominant effects on the local $k_i$ solutions along the kinked crack front. Here, we lump all the effects of geometry and loading of the specimen to the distributions of the global stress intensity factor $K_i$ solutions along the main crack front.

As indicated in Wang et al. (in press) for lap-shear specimens, the global stress intensity factor $K_i$ solutions can be influenced by the geometry of the specimen, namely,

$$K_i = K_i(\theta, t, b, t/b, W/b, V/b, L/b), \quad i = \mathrm{I}, \mathrm{II}, \mathrm{III} \tag{5}$$

Therefore, in order to accurately investigate and specify the local $k_i$ solutions of kinked cracks in spot weld specimens, the number of cases needed to be considered is rather large. In this investigation, we will concentrate on the local $k_i$ solutions at the maximum kink depths for several kink depths, a given aspect ratio $d/c$ of the semi-elliptical kinked crack, and a specific specimen geometry of Lin et al. (in press). Our goals are to understand the general effects of the finite kink depth on the local $k_i$ solutions and the link between the local $k_i$ solutions for finite kink depths and the local $k_i$ solutions for vanishing kink depth based on the global $K_i$ solutions and the analytical kink crack solutions in Eqs. (1) and (2).

Note that the local stress intensity factor solutions for kinked cracks with several kink depths in lap-shear specimens were obtained in Pan and Sheppard (2003) for their lap-shear and modified coach peel specimens. But the solutions are not presented in terms of the closed-form kinked crack solutions. Note that Newman and Dowling (1998), Lin and Pan (2004) and Lin et al. (in press) adopted the closed-form local stress intensity factor solution for kinked cracks with a vanishing kink depth in their two-dimensional fatigue model to estimate the fatigue lives of spot welds in lap-shear specimens. Recently, due to advancement of friction stir welding technology, continuous lap joints were produced for aluminum sheets (Scafe and Joaquin, 2004). The fatigue life analyses of these continuous lap joints based on the local stress intensity factor solutions for kinked cracks are also needed. Therefore, we also examine the local stress intensity factor solutions for kinked cracks with several kink depths based on a two-dimensional plane-strain finite element model.

## 3. A finite element analysis with no kinked crack

### 3.1. Three-dimensional finite element model

In order to obtain the local stress intensity factor solutions for kinked cracks with a vanishing kink depth, a three-dimensional finite element analysis is first carried out to obtain the global stress intensity

factor solutions for the crack front along the nugget circumference. The finite element model for lap-shear specimens is evolved from the three-dimensional finite element model for two circular plates with connection, where a mesh sensitivity study was carried out to benchmark the global stress intensity factor solution to a closed-form solution under axisymmetric loading conditions (Wang et al., 2005). The details to select an appropriate three-dimensional mesh for obtaining accurate stress intensity factor solutions for spot welds can be found in Wang et al. (2005) and Wang et al. (in press).

Due to symmetry, only a half lap-shear specimen is considered. Fig. 5(a) shows a schematic plot of a half lap-shear specimen. The specimen has the sheet thickness $t$ (=0.65 mm), the length $L$ (=77.3 mm), the half width $W$ (=18.9 mm), and the nugget radius $b$ (=3.2 mm) according to the dimensions of the lap-shear specimens used in Lin et al. (in press). The overlap length $V$ of the upper and lower sheets is 47.1 mm. The two spacers have the length $S$ (=4.6 mm). Both the upper and lower sheets have the same thickness. A Cartesian coordinate system is also shown in the figure. As shown in Fig. 5(a), a uniform displacement is applied in the $-x$ direction to the left edge surface of the specimen, and the displacements in the $x$, $y$ and $z$ directions for the right edge surface of the specimen are constrained to represent the clamped boundary conditions in the experiment. The displacement in the $y$ direction of the symmetry plane, the $x$–$z$ plane, is constrained to represent the symmetry conditions due to the loading conditions and the geometry of the specimen. Fig. 5(b) shows a mesh for a left half finite element model. Fig. 5(c) shows a close-up view of the mesh near the main crack tip. Note that the main crack is modeled as a sharp crack here. The three-dimensional finite element mesh near the weld nugget is evolved from the three-dimensional finite element mesh for two circular plates with connection as discussed in Wang et al. (2005). As shown in Fig. 5(c), the

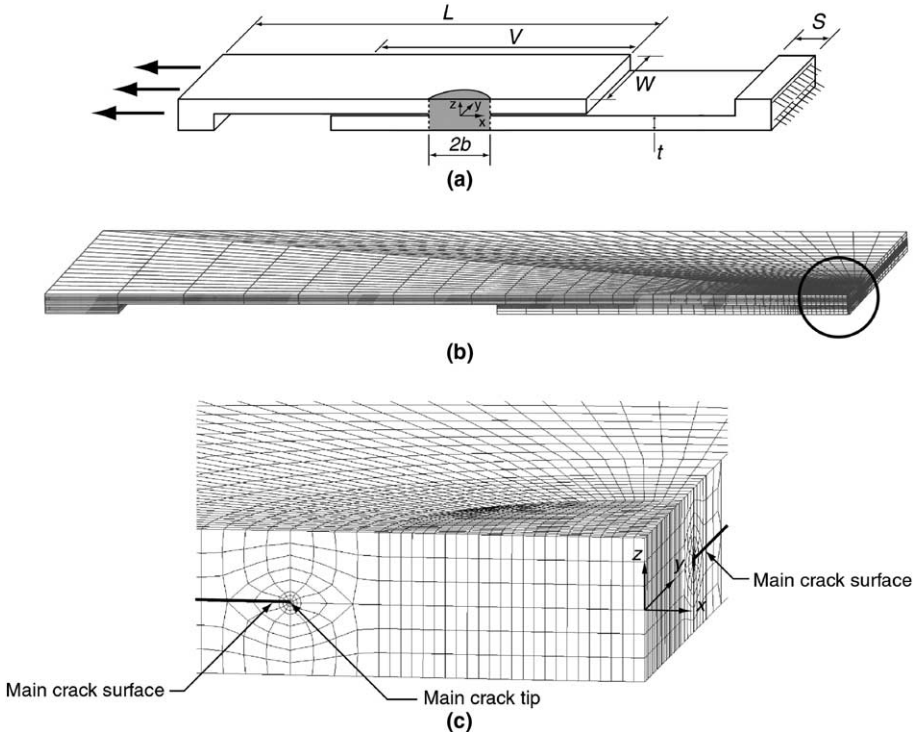


Fig. 5. (a) A schematic plot of a half lap-shear specimen with a uniform displacement applied to the left edge surface of the specimen shown as the bold arrows and the clamped boundary conditions for the right edge surface of the specimen. The shaded region represents the half weld nugget. (b) A mesh for a left half finite element model. (c) A close-up view of the mesh near the main crack tip.

mesh near the center of the weld nugget is refined to ensure reasonable aspect ratios of the three-dimensional brick elements. The three-dimensional finite element model for the half lap-shear specimen has 34,248 20-node quadratic brick elements. The main crack surfaces are also shown as bold lines in Fig. 5(c).

In this investigation, the weld nugget and the base metal are assumed to be linear elastic isotropic materials. The Young's modulus $E$ is taken as 200 GPa, and the Poisson's ratio $v$ is taken as 0.3. The commercial finite element program ABAQUS (Hibbitt et al., 2001) is employed to perform the computations. Brick elements with quarter point nodes and collapsed nodes along the crack front are used to model the $1/\sqrt{r}$ singularity near the crack tip. The computational stress intensity factor solutions are obtained based on the interaction integral method for cracks under mixed-mode loading conditions (Shih and Asaro, 1988). The stress intensity factor solutions are directly computed by ABAQUS.

First, the distributions of the global stress intensity factor solutions along the circumference of the nugget are examined here. Fig. 6 shows a top view of a nugget with a cylindrical coordinate system centered at the nugget center. An orientation angle $\theta$ is measured counterclockwise from the critical location of point B. Fig. 7 shows the normalized $K_{\mathrm{I}}$, $K_{\mathrm{II}}$ and $K_{\mathrm{III}}$ solutions as functions of $\theta$ for the crack front along the nugget circumference based on our three-dimensional finite element computations for the lap-shear specimen with $t/b = 0.2$, $W/b = 5.91$, $V/b = 14.72$ and $L/b = 24.16$ (Wang et al., in press). Note that the $K_{\mathrm{I}}$, $K_{\mathrm{II}}$ and $K_{\mathrm{III}}$ solutions are normalized by the $K_{\mathrm{II}}$ solution at the critical location of point A ($\theta = 180°$). Due to the symmetry, we only show the results from $\theta = 0°$ to 180°. As shown in Fig. 7, the maxima of the $K_I$ solution are located at point B ($\theta = 0°$) and point A ($\theta = 180°$), the maximum and minimum of the $K_{\mathrm{II}}$ solution are located at point A ($\theta = 180°$) and point B ($\theta = 0°$), respectively, and the maximum of the $K_{\mathrm{III}}$ solution is located at point D ($\theta = 90°$). The results shown in Fig. 7 indicate that the global $K_{\mathrm{II}}$ is the dominant global stress intensity factor in lap-shear specimens under shear dominant loading conditions. The distributions of the global stress intensity factor solutions along the circumference of the nugget as shown in Fig. 7 are similar to those in Radaj et al. (1990). The results shown in Fig. 7 were also reported in Wang et al. (in press). The results shown in Fig. 7 will be used as the basis to report the local stress intensity factor solutions for kinked cracks with vanishing kink depth. Note that Lin et al. (to be submitted for publication) recently derived the $K_{\mathrm{I}}$ solution for a spot weld connecting at the center of two square plates under an applied counter bending moment $M_0$ along the two edges of each plate per unit length as

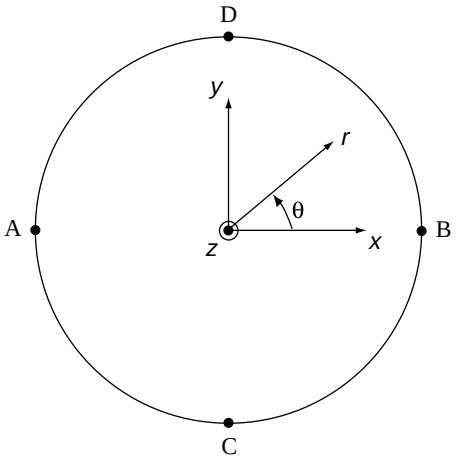


Fig. 6. A top view of a nugget with an orientation angle $\theta$ defined as shown. See Fig. 4(a) for the locations of points A–D.

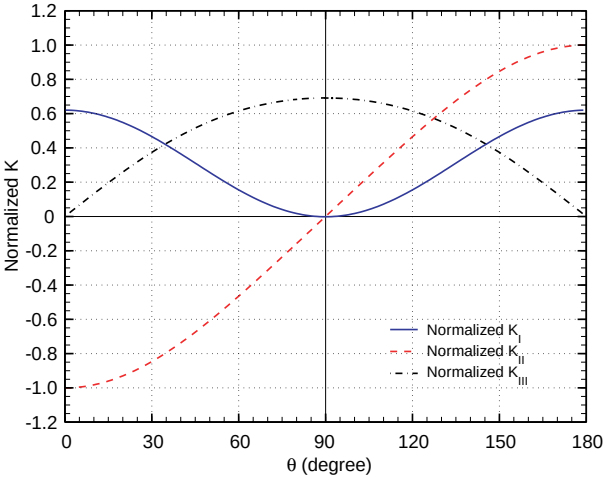


Fig. 7. The normalized $K_{\mathrm{I}}$, $K_{\mathrm{II}}$ and $K_{\mathrm{III}}$ solutions as functions of $\theta$ for the crack front along the nugget circumference based on our three-dimensional finite element computations for the lap-shear specimen used in Lin et al. (in press).

$$K_{\mathrm{I}} = \frac{M_0\sqrt{3}}{t\sqrt{tXY}}\{X[Y - b^2(-1+v) + W^2(-1+v)] - Y[-X + b^8(-1+v) + 2b^4W^4(1+v) - 4b^2W^6(1+v) + W^8(3+v)]\}\cos(2\theta) \tag{6}$$

where $b$ is the radius of the spot weld, $t$ is the thickness of the plate, $2W$ is the width of the plate, and $v$ is the Poisson's ratio of the plate material. Here, $X$ and $Y$ are defined as

$$X = (-1+v)(b^4 + W^4)^2 - 4b^2W^6(1+v) \tag{7}$$

$$Y = b^2(-1+v) - W^2(1+v) \tag{8}$$

The maximum magnitude of $K_{\mathrm{I}}$ is located at $\theta = 0°$ (point B) and $\theta = 180°$ (point A). The details for the derivation of the $K_{\mathrm{I}}$ solution in Eq. (6) are reported in Lin et al. (to be submitted for publication).

### 3.2. Local stress intensity factor solutions for vanishing kink depth

Fig. 8 shows the normalized local $k_{\mathrm{I}}$, $k_{\mathrm{II}}$ and $k_{\mathrm{III}}$ solutions as functions of $\theta$ for the crack front from $\theta = 90°$ to 180° along the nugget circumference of the lap-shear specimen. We only examine this range of $\theta$ since the local $k_{\mathrm{I}}$ solution from $\theta = 90°$ to 270° is positive for the loading condition shown in Fig. 5(a). The local $k_{\mathrm{I}}$, $k_{\mathrm{II}}$ and $k_{\mathrm{III}}$ solutions are determined from the global $K_{\mathrm{I}}$, $K_{\mathrm{II}}$ and $K_{\mathrm{III}}$ solutions based on our three-dimensional finite element computations and the analytical kinked crack solutions in Eqs. (1)–(3) with the kink angle $\alpha = 90°$. The cylindrical coordinate system $(r, \theta, z)$ which is used to describe the orientation of $\theta$ is shown in Fig. 6. Note that the local $k_{\mathrm{I}}$, $k_{\mathrm{II}}$ and $k_{\mathrm{III}}$ solutions are normalized by the local $k_{\mathrm{I}}$ solution at the critical location of point A ($\theta = 180°$). As shown in Fig. 8, the maximum of the local $k_{\mathrm{I}}$ solution is located at the critical location of point A ($\theta = 180°$). Therefore, a small kinked crack can emanate from point A ($\theta = 180°$) and grow to the sheet surface of the specimen due to the high value of the local $k_{\mathrm{I}}$. Note that the maximum of the local $k_{\mathrm{II}}$ solution is also located at the critical location of point A ($\theta = 180°$). Note that for a given mixture of $K_{\mathrm{I}}$ and $K_{\mathrm{II}}$ or a given ratio of $K_{\mathrm{I}}$ to $K_{\mathrm{II}}$, a kink angle $\alpha$ can be found such that the local $k_{\mathrm{I}}$ is maximum and the local $k_{\mathrm{II}}$ is 0 (Pook, 1975; Newman and Dowling, 1998; Lin and Pan, 2004). A kinked crack with this kink angle $\alpha$ can grow under pure local mode I conditions. However, due to

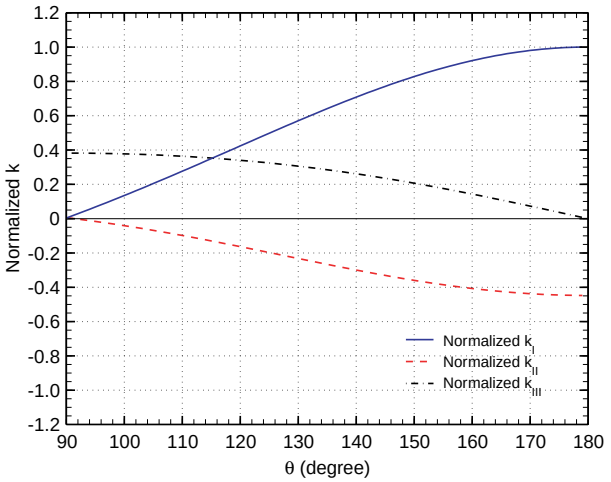


Fig. 8. The normalized $k_I$, $k_{II}$ and $k_{III}$ solutions as functions of $\theta$ for the crack front along the nugget circumference based on our three-dimensional finite element computations and the analytical kinked crack solutions in Eqs. (1)–(3) with the kink angle $\alpha = 90°$.

different crack growth resistances for different microstructures near the main crack, the kinked crack grows in the direction of the least fatigue resistance. Based on the experimental observations, the kink angle $\alpha$ for kinked fatigue cracks appears to be close to 90° in lap-shear specimens (Lin et al., to be submitted for publication).

## 4. Finite element analyses for finite kinked cracks

### 4.1. Three-dimensional finite element models

After a kinked crack emanating from the main crack, the local stress intensity factor solutions at the kinked crack tip are different from the global stress intensity factor solutions for the main crack in lap-shear specimens under the applied loading condition. This general trend was shown for cup specimens based on axisymmetric finite element analyses in Wang et al. (2005). Here, three-dimensional finite element models are employed to investigate the local stress intensity factor solutions for kinked cracks with different kink depths in lap-shear specimens. Four maximum kink depths are considered, namely, $d/t = 0.05$, 0.2, 0.5 and 0.7. Here, $d$ and $t$ represent the maximum kink depth and the specimen thickness, respectively. Note that according to the experimental observations of Swellam et al. (1992), kinked cracks can form at the critical locations (either point A or point B as shown in Fig. 4(a)) in a lap-shear specimen. However, a single kinked crack usually became dominant and resulted in the specimen failure. In our finite element models for lap-shear specimens, only one kinked crack emanating from the main crack is modeled on one side of the weld nugget in the specimen.

Fig. 9(a) again shows a schematic plot of a half lap-shear specimen. The specimen has the same dimensions as those of the lap-shear specimens used in Lin et al. (in press) as discussed earlier. The two spacers have the length $S$ (=4.6 mm). The nugget radius $b$ is 3.2 mm. Both the upper and lower sheets have the same thickness. The kinked crack front with the maximum kink depth $d$ is shown as dashed lines in the figure. Fig. 9(a) also shows the loading and boundary conditions applied to the lap-shear specimen. The loading, boundary and symmetry conditions of the half specimen are the same as those discussed earlier for Fig. 5(a).

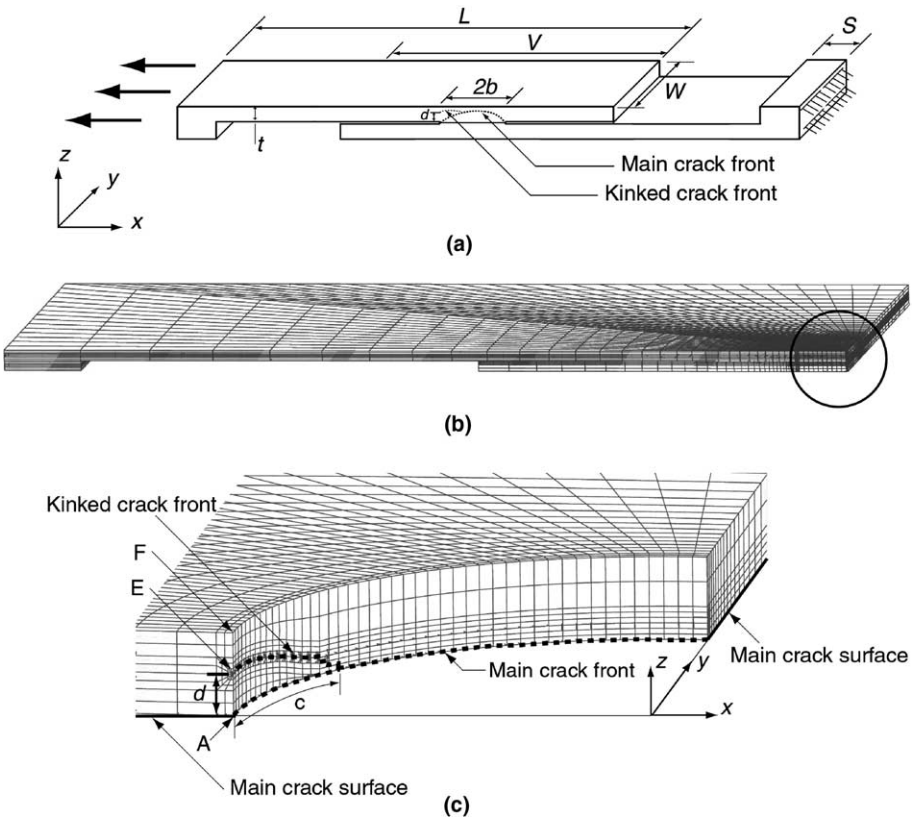


Fig. 9. (a) A schematic plot of a half lap-shear specimen with a uniform displacement applied to the left edge surface of the specimen shown as the bold arrows and the clamped boundary conditions of the right edge surface of the specimen. (b) A mesh for a left half three-dimensional finite element model. (c) A close-up view of the mesh near the kinked crack.

The mesh for a left half finite element model with $d/t = 0.5$ is shown in Fig. 9(b). A close-up view of the mesh near the kinked crack is shown in Fig. 9(c). The aspect ratio of the maximum kink depth $d$ to the half length $c$ along the nugget circumference for the semi-elliptical kinked crack is taken as 0.4 as in Pan and Sheppard (2003). As shown in Fig. 9(c), the mesh of the weld nugget is removed to display the mesh for the kinked crack clearly. The main crack and the kinked crack fronts are shown as dashed lines in the figure. The main crack surfaces are shown as solid lines in the figure. The three-dimensional finite element mesh near the nugget is based on the three-dimensional finite element model for two circular plates with connection as discussed in Wang et al. (2005). The three-dimensional finite element model for a half lap-shear specimen with the kinked crack for $d/t = 0.5$ has 56,172 20-node quadratic brick elements.

### 4.2. Two-dimensional plane-strain finite element models

Investigation of the local stress intensity factor solutions for kinked cracks in lap-shear specimens by three-dimensional finite element analyses is computationally intensive and tedious. In order to investigate the applicability of two-dimensional finite element analyses to obtain the local stress intensity factor solutions for kinked cracks in lap-shear specimens, two-dimensional plane-strain finite element models are developed. The common parameters of the two-dimensional and three-dimensional models are the sheet

thickness $t$, the specimen length $L$, the overlap length $V$ and the length of two spacers $S$. The weld nugget in the three-dimensional model has a radius $b$ whereas the weld in the two-dimensional plane-strain model has a size $2b$. Four kink depths are considered, namely, $d/t = 0.05$, 0.2, 0.5 and 0.7. Here, $d$ and $t$ represent the kink depth and the specimen thickness, respectively. The main crack is modeled as a sharp crack. Note that continuous lap joints of two aluminum sheets by friction stir welding have been used to produce automotive components (Scafe and Joaquin, 2004). Therefore, the local stress intensity factor solutions for kinked cracks obtained from the two-dimensional finite element analysis are also useful to assess the fatigue lives of the continuous lap joints.

Fig. 10(a) shows a schematic plot of a lap-shear specimen. The specimen has the sheet thickness $t$ (=0.65 mm), the length $L$ (=77.3 mm) and the nugget radius $b$ (=3.2 mm) according to the dimensions of the symmetry cross-section of the lap-shear specimens used in Lin et al. (in press). Both the upper and lower sheets have the same thickness. The length $S$ of the two spacers is 4.6 mm, and the overlap length $V$ of the upper and lower sheets is 47.1 mm. A kinked crack is shown as dashed lines in the figure. Note that the two-dimensional plane-strain finite element model has a unit length in the width direction. Fig. 10(a) also shows the loading and boundary conditions applied to the two-dimensional plane-strain finite element model. A Cartesian coordinate system is also shown in the figure. As shown in Fig. 10(a), the displacements

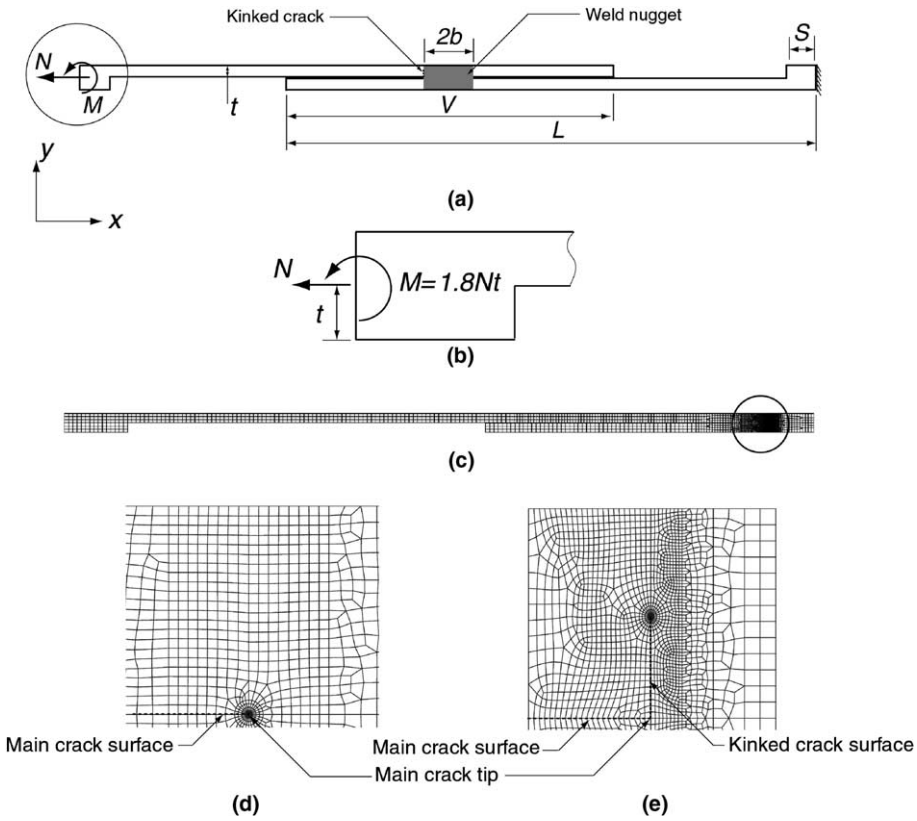


Fig. 10. (a) A schematic plot of a lap-shear specimen with the applied loads and the boundary conditions. (b) A schematic plot of the loading condition near the left edge surface of the specimen. (c) A mesh of the left part of the two-dimensional plane-strain finite element model with $d/t = 0.5$. (d) A close-up view of the mesh near the main crack tip for the model with $d/t = 0$. (e) A close-up view of the mesh near the main crack tip for the model with $d/t = 0.5$.

in the $x$ and $y$ directions for the right edge surface of the specimen are constrained to represent the clamped boundary conditions. A concentrated load $N$ and a moment $M$ ($=1.8Nt$) per unit width are applied in the $-x$ direction and counterclockwise, respectively, to the center of the left edge surface of the specimen. Fig. 10(b) is a schematic plot of the loading condition near the left edge surface of the specimen of the two-dimensional plane-strain finite element model. The moment is applied through two concentrated forces of the same magnitude but in the opposite directions of $x$ and $-x$ at the equal distance to the mid-plane of the left edge surface. Under this combination of $N$ and $M$, the value of the global stress intensity factor ratio $K_{\mathrm{I}}/K_{\mathrm{II}}$ is 0.62 for the two-dimensional plane-strain finite element model with $d/t = 0$. This ratio is the same as that at the critical locations of the corresponding three-dimensional finite element model with $d/t = 0$. The mesh of the left part of the two-dimensional plane-strain finite element model for the lap-shear specimen with $d/t = 0.5$ is shown in Fig. 10(c). Close-up views of the meshes near the main crack tips for the lap-shear specimens with $d/t = 0$ and 0.5 are shown in Fig. 10(d) and (e), respectively. The main crack surface and kinked crack surface are shown as dashed lines in the figure.

### 4.3. Computational results for kinked cracks

The normalized maximum local $k_{\mathrm{I}}$ and $k_{\mathrm{II}}$ solutions at point E of the maximum kink depth (as shown in Fig. 9(c)) for the lap-shear specimen are plotted as functions of the normalized maximum kink depth $d/t$ in Figs. 11 and 12, respectively. The maximum local $k_{\mathrm{I}}$ and $k_{\mathrm{II}}$ solutions are normalized by $(k_{\mathrm{I}})_{0,3\mathrm{D\,FEM}}$. Here, $(k_{\mathrm{I}})_{0,3\mathrm{D\,FEM}}$ is the local $k_{\mathrm{I}}$ solution for vanishing kink depth based on our three-dimensional finite element computation for the lap-shear specimen with $d/t = 0$ and the analytical kinked crack solution in Eq. (1) with the kink angle $\alpha = 90°$. The normalized local $k_{\mathrm{I}}$ and $k_{\mathrm{II}}$ solutions for the two-dimensional lap-shear specimen are also plotted as functions of the normalized kink depth $d/t$ in Figs. 11 and 12, respectively. For the two-dimensional lap-shear specimens, the local $k_{\mathrm{I}}$ and $k_{\mathrm{II}}$ solutions are normalized by $(k_{\mathrm{I}})_{0,2\mathrm{D\,FEM}}$. Here, $(k_{\mathrm{I}})_{0,2\mathrm{D\,FEM}}$ is the local $k_{\mathrm{I}}$ solution for vanishing kink depth based on our two-dimensional plane-strain finite element computation for the lap-shear specimen with $d/t = 0$ and the analytical kinked crack solution in Eq. (1) with the kink angle $\alpha = 90°$.

Fig. 11 shows that when the maximum kink depth approaches to 0, the local $k_{\mathrm{I}}$ solutions based on our three-dimensional and two-dimensional plane-strain finite element computations appear to approach to

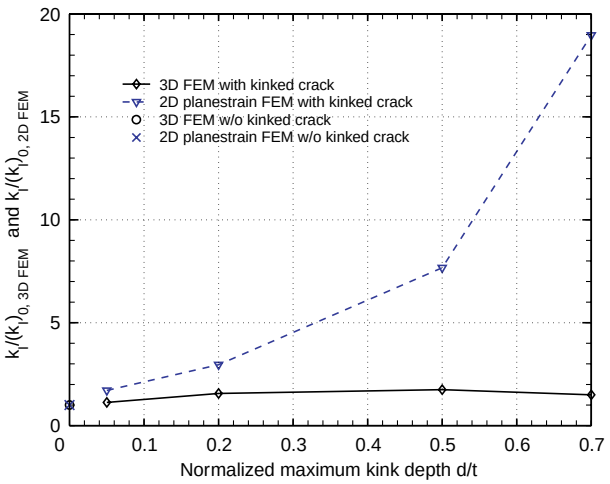


Fig. 11. The normalized local $k_{\mathrm{I}}$ solutions as functions of the normalized maximum kink depth $d/t$ based on our three-dimensional and two-dimensional plane-strain finite element computations for the lap-shear specimen.

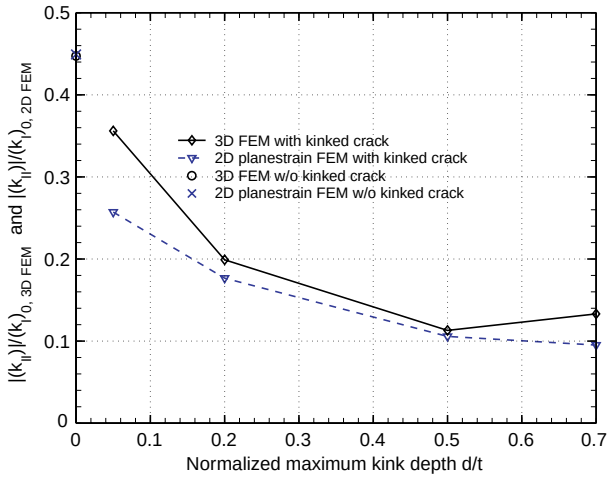


Fig. 12. The magnitudes of the normalized $k_{II}$ solutions as functions of the normalized maximum kink depth $d/t$ based on our three-dimensional and two-dimensional plane-strain finite element computations for the lap-shear specimen.

$(k_I)_{0,3D\,FEM}$ and $(k_I)_{0,2D\,FEM}$, respectively. Fig. 11 also shows that the maximum local $k_I$ solution based on our three-dimensional finite element computations increases as the maximum kink depth increases to a half sheet thickness. As the maximum kink depth further increases to 70% of the sheet thickness, the maximum local $k_I$ solution based on our three-dimensional finite element computations decreases slightly. However, the local $k_I$ solution based on our two-dimensional plane-strain finite element computations increases monotonically as the kink depth increases to 70% of the sheet thickness. Since the local $k_I$ solution based on our two-dimensional plane-strain finite element computations does not correlate with that based on our three-dimensional finite element computations, the kinked crack model based on our two-dimensional plane-strain finite element model for the lap-shear specimen may not be appropriate to be used for estimation of the local $k_I$ solution for the three-dimensional kinked cracks. Note that for the three-dimensional kinked crack model, as the maximum kink depth increases, the local load carrying capacity of the remaining ligament EF (as shown in Fig. 9(c)) at the critical location possibly decreases due to the redistribution of the load carrying capacity to the remaining ligament of the entire kinked crack front and the entire circumference of the nugget. However, for the two-dimensional kinked crack model, redistribution of the local load carrying capacity cannot occur. Therefore, the local $k_I$ solution based on the two-dimensional finite element computations increases substantially as the kink depth increases.

It should be noted that based on the results presented in Fig. 11, the two-dimensional plane-strain model may not be appropriate for the lap-shear spot weld specimen. However, it can be used to model the kinked cracks emanating from continuous lap joints made by the new friction stir welding technology for aluminum sheets (Scafe and Joaquin, 2004). The local stress intensity factor solutions obtained here for kinked cracks with several kink depths based on the two-dimensional plane-strain finite element model can be applied to the fatigue life predictions of these continuous lap joints.

Note that according to the definition of the local $k_{II}$ specified in Fig. 1, the local $k_{II}$ is negative. Fig. 12 shows that the magnitude of the local $k_{II}$ solution based on our three-dimensional finite element computations decreases as the maximum kink depth increases to a half sheet thickness and increases slightly as the maximum kink depth further increases to 70% of the sheet thickness. On the other hand, the magnitude of the local $k_{II}$ solution based on our two-dimensional plane-strain finite element computations decreases monotonically as the maximum kink depth increases from 0% to 70% of the sheet thickness. Fig. 12 also shows that when the maximum kink depth approaches to 0, the magnitude of the local $k_{II}$ solution based on

our three-dimensional finite element computations appears to approach to that for vanishing kink depth based on our three-dimensional finite element computation for $d/t = 0$ and the analytical kinked crack solution in Eq. (2) with the kink angle $\alpha = 90°$. However, as shown in Fig. 12, when the kink depth approaches to 0, the magnitude of the local $k_{II}$ solution based on our two-dimensional plane-strain finite element computations appears not to approach quickly to that for vanishing kink depth based on our two-dimensional plane-strain finite element computation for $d/t = 0$ and the analytical kinked crack solution in Eq. (2) with $\alpha = 90°$. Theoretically speaking, as $d/t$ decreases, the magnitude of the local $k_{II}$ solution based on our two-dimensional plane-strain finite element computations should approach to that for vanishing kink depth based on our two-dimensional plane-strain finite element computation for $d/t = 0$ and the analytical kinked crack solution in Eq. (2) with $\alpha = 90°$. However, the approach to the theoretical value appears to be quite slowly for this case (Wang et al., 2005).

For potential future applications, Table 1 lists the normalized maximum local $k_I$ and $k_{II}$ solutions at the critical locations (point A and point B as shown in Fig. 4(a)) based on our three-dimensional finite element computations and the analytical kinked crack solutions in Eqs. (1) and (2) with the kink angle $\alpha = 90°$. Table 2 lists the normalized local $k_I$ and $k_{II}$ solutions based on our two-dimensional plane-strain finite element computations under the combined load of $N$ and $M$ ($=1.8Nt$). For completeness, Tables 3 and 4 list the normalized local $k_I$ and $k_{II}$ solutions based on our two-dimensional plane-strain finite element computations under pure $N$ and pure $M$ loading conditions, respectively. As listed in Tables 2–4, when the normalized kink depth increases, the normalized local $k_I$ solution increases substantially. The details on the global $K_I$ and $K_{II}$ solutions for continuous lap joints can be found in Lin et al. (to be submitted for publication). Based on the superposition principle of linear elasticity, when the global $K_I$ and $K_{II}$ solutions are

Table 1
The normalized maximum local $k_I$ and $k_{II}$ solutions at the critical locations (points A and B as shown in Fig. 4(a)) for several values of the normalized maximum kink depth $d/t$ based on our three-dimensional finite element computations and the analytical kinked crack solutions in Eqs. (1) and (2) with the kink angle $\alpha = 90°$

| $d/t$ | 0 | 0.05 | 0.2 | 0.5 | 0.7 |
|---|---|---|---|---|---|
| $k_I/(k_I)_{0,3D\,FEM}$ | 1.00 | 1.13 | 1.56 | 1.75 | 1.49 |
| $k_{II}/(k_I)_{0,3D\,FEM}$ | −0.45 | −0.36 | −0.20 | −0.11 | −0.13 |

Table 2
The normalized local $k_I$ and $k_{II}$ solutions for several values of the normalized kink depth $d/t$ based on our two-dimensional plane-strain finite element computations and the analytical kinked crack solutions in Eqs. (1) and (2) with the kink angle $\alpha = 90°$ under the combined load of $N$ and $M$ ($=1.8Nt$)

| $d/t$ | 0 | 0.05 | 0.2 | 0.5 | 0.7 |
|---|---|---|---|---|---|
| $k_I/(k_I)_{0,2D\,FEM}$ | 1.00 | 1.71 | 2.96 | 7.69 | 18.97 |
| $k_{II}/(k_I)_{0,2D\,FEM}$ | −0.45 | −0.26 | −0.18 | −0.11 | −0.10 |

Table 3
The normalized local $k_I$ and $k_{II}$ solutions for several values of the normalized kink depth $d/t$ based on our two-dimensional plane-strain finite element computations and the analytical kinked crack solutions in Eqs. (1) and (2) with the kink angle $\alpha = 90°$ under pure $N$ ($M = 0$) loading conditions

| $d/t$ | 0 | 0.05 | 0.2 | 0.5 | 0.7 |
|---|---|---|---|---|---|
| $k_I/(k_I)_{0,2D\,FEM}$ | 1.00 | 1.62 | 2.58 | 5.86 | 12.80 |
| $k_{II}/(k_I)_{0,2D\,FEM}$ | −0.49 | −0.30 | −0.20 | −0.07 | −0.02 |

Table 4
The normalized local $k_I$ and $k_{II}$ solutions for several values of the normalized kink depth $d/t$ based on our two-dimensional plane-strain finite element computations and the analytical kinked crack solutions in Eqs. (1) and (2) with the kink angle $\alpha = 90°$ under pure $M$ ($N = 0$) loading conditions

| $d/t$ | 0 | 0.05 | 0.2 | 0.5 | 0.7 |
|---|---|---|---|---|---|
| $k_I/(k_I)_{0,2D\,FEM}$ | 1.00 | 1.57 | 2.35 | 4.79 | 9.12 |
| $k_{II}/(k_I)_{0,2D\,FEM}$ | −0.52 | −0.33 | −0.21 | −0.05 | 0.02 |

available for a given combination of $N$ and $M$, the local $k_I$ and $k_{II}$ solutions for various kink depths can be estimated from the normalized solutions listed in Tables 3 and 4. Note that for the given direction of $M$ as shown in Fig. 10(b), the local $k_I$ solutions for various kink depths are negative. The direction of $M$ is needed to give the ratio $K_I/K_{II} = 0.62$. The details will be explained in Lin et al. (to be submitted for publication).

It should be noted that for semi-elliptical kinked cracks emanating from the main crack, the maximum values of the local $k_I$ and $k_{II}$ solutions occur at point E (as shown in Fig. 9(c)). As indicated in Eqs. (4) and (5), the local $k_I$ and $k_{II}$ solutions are affected by the global $K_I$, $K_{II}$ and $K_{III}$ solutions which are in turn affected by the geometry of the specimen. In our investigation, we have selected $t/b = 0.20$, $d/c = 0.40$, $W/b = 5.91$, $V/b = 14.72$ and $L/b = 24.16$. Note that Pan and Sheppard (2003) obtained the local $k_I$ and $k_{II}$ solutions for $t/b = 0.47$, $d/c = 0.40$, $W/b = 5.50$, $V/b = 10$ and $L/b = 21$. Figs. 13 and 14 show comparisons of the normalized local $k_I$ and $k_{II}$ solutions based on our three-dimensional finite element computations and the three-dimensional finite element computations of Pan and Sheppard (2003). Our computational local $k_I$ and $k_{II}$ solutions are normalized by the local $k_I$ solution for vanishing kink depth based on our computational global $K_I$ and $K_{II}$ solutions for $d/t = 0$ and the analytical kinked crack solution in Eq. (1) with the kink angle $\alpha = 90°$. Note that Pan and Sheppard (2003) used the surface crack solution of Newman and Raju (1981) to fit their computational solutions. For a fair comparison, the computational local $k_I$ and $k_{II}$ solutions of Pan and Sheppard (2003) are now normalized by the local $k_I$ solution for vanishing kink depth based on the global $K_I$ and $K_{II}$ solutions of Pan and Sheppard (2003) for $d/t = 0$ and the analytical kinked crack solution in Eq. (1) with the kink angle $\alpha = 90°$. Here, we link the local $k_I$ and $k_{II}$ solutions for the kinked cracks with different kink depths to those for vanishing kink depth based on the global $K_I$ and $K_{II}$ solutions for $d/t = 0$ and the analytical kinked crack solutions in Eqs. (1) and (2).

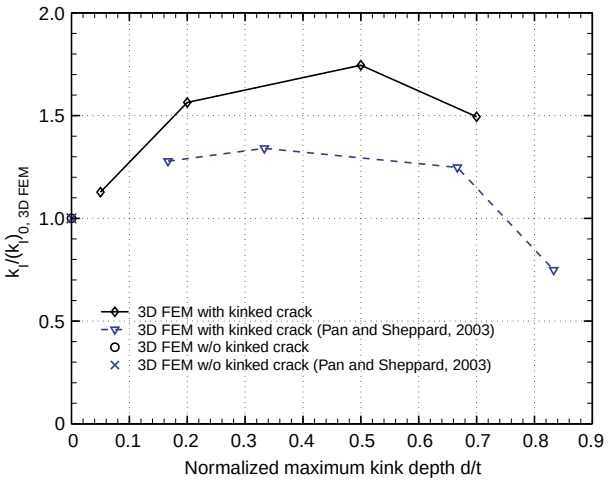


Fig. 13. The normalized local $k_I$ solutions as functions of the normalized maximum kink depth $d/t$ based on our three-dimensional finite element computations and the three-dimensional finite element computations of Pan and Sheppard (2003).

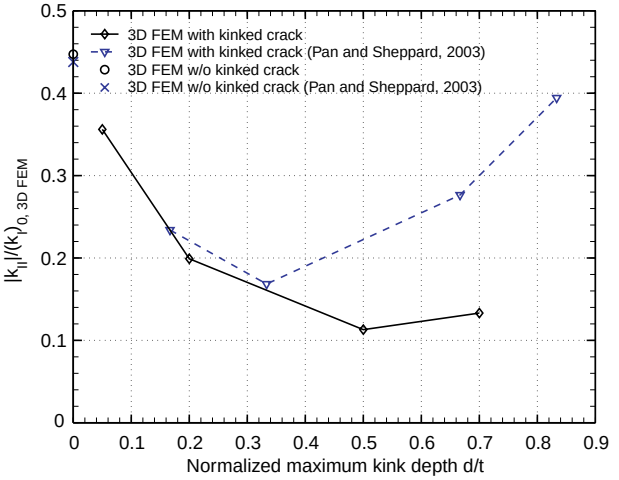


Fig. 14. The magnitudes of the normalized local $k_{II}$ solutions as functions of the normalized maximum kink depth $d/t$ based on our three-dimensional finite element computations and the three-dimensional finite element computations of Pan and Sheppard (2003).

As shown in Fig. 13, when the normalized maximum kink depth $d/t$ approaches to 0, the local $k_I$ solutions based on our three-dimensional finite element computations and those based on the three-dimensional finite element computations of Pan and Sheppard (2003) appear to approach to our local $k_I$ solution and the local $k_I$ solution of Pan and Sheppard (2003) for $d/t = 0$, respectively. As the normalized maximum kink depth $d/t$ increases, the local $k_I$ solutions based on our three-dimensional finite element computations and the three-dimensional finite element computations of Pan and Sheppard (2003) increase then decrease. The general trend of our computational $k_I$ solution is the same as that of Pan and Sheppard (2003). Based on our three-dimensional finite element computations, the critical local mode I stress intensity factor solution can increase up to 75% as the maximum kink depth increases to a half sheet thickness, and then decreases slightly as the maximum kink depth further increases to 70% of the sheet thickness. But the increase of the critical local mode I stress intensity factor solutions of Pan and Sheppard (2003) is not as high as our computational results. Note that we normalize the $k_I$ solutions by the $k_I$ solution for the kinked crack with vanishing kink depth based on the global stress intensity factor solutions. If we concentrate on the effects of the kinked crack geometries for the two cases, the major difference for the two cases is that the angular span $c/b$ is larger for the kinked crack model of Pan and Sheppard (2003) due to the large ratio of $t/b$ for the same normalized maximum kink depth $d/t$. Note that the kinked cracks of the two cases have the same aspect ratio $d/c$. However, without a systematic analysis, no conclusion can be made from the available two sets of solutions.

As shown in Fig. 14, when the normalized maximum kink depth $d/t$ approaches to 0, the magnitude of the local $k_{II}$ solutions based on our three-dimensional finite element computations and those based on the three-dimensional finite element computations of Pan and Sheppard (2003) appear to approach to our local $k_{II}$ solution and the local $k_{II}$ solution of Pan and Sheppard (2003) for $d/t = 0$, respectively. As the normalized maximum kink depth $d/t$ increases, the magnitudes of the local $k_{II}$ solutions based on our three-dimensional finite element computations and the three-dimensional finite element computations of Pan and Sheppard (2003) decrease then increase. The general trend of our computational $k_{II}$ solution is the same as that of Pan and Sheppard (2003).

Note that a mesh sensitivity study for the finite element model with no kinked cracks used in this investigation has been performed in Wang et al. (2005). The global stress intensity factor solution based on the finite element model was well benchmarked to the analytical solution for circular plates with connection

and cylindrical cup specimens under axisymmetric loading conditions. Also, the finite element models with no kinked cracks used in this investigation were used to investigate the specimen size effects on the global stress intensity factor solutions in Wang et al. (in press). The computational results indicate that when the spot weld becomes small compared to the width, length, and overlap length of the specimen, the stress intensity factor solutions are in agreement with the analytical solutions. Moreover, when the kink length decreases to zero, the stress intensity factor solutions for kinked cracks based on the finite element models with kinked cracks were shown be consistent with those based on the global stress intensity solutions and the analytical solutions in Wang et al. (in press).

On the other hand, Pan and Sheppard (2003) used the sub-modeling technique in ABAQUS (Hibbitt et al., 2001) to obtain their stress intensity factor solutions. Pan and Sheppard (2003) did not report a mesh sensitivity study and did not examine the accuracy of their global or local stress intensity factor solutions with respect to known analytical solutions. However, the geometric factors such as $t/b$, $W/b$, $L/b$, and $V/b$ are different for the specimens of Lin et al. (in press) and Pan and Sheppard (2003). Therefore, the global and local stress intensity factor solutions can be different. But the most important feature shown in Figs. 13 and 14 is that the general trends of the local $k_{\mathrm{I}}$ and $k_{\mathrm{II}}$ solutions are quite similar for the specimens of Lin et al. (in press) and Pan and Sheppard (2003).

## 5. Conclusions and discussions

Three-dimensional and two-dimensional plane-strain finite element analyses are carried out to investigate the local stress intensity factor solutions for kinked cracks with various kink depths in lap-shear specimens. The local stress intensity factor solutions at the critical locations of the kinked cracks are obtained. The computational local stress intensity factor solutions at the critical locations of the kinked cracks of finite depths are expressed in terms of those for vanishing kink depth based on the global stress intensity factor solutions and the analytical kinked crack solutions for vanishing kink depth. The three-dimensional finite element computational results show that the critical local mode I stress intensity factor solution increases and then decreases as the kink depth increases. When the kink depth approaches to 0, the critical local mode I stress intensity factor solution appears to approach to that for vanishing kink depth based on the global stress intensity factor solutions and the analytical kinked crack solutions for vanishing kink depth. The two-dimensional plane-strain computational results indicate that the critical local mode I stress intensity factor solution increases monotonically and increases substantially more than that based on the three-dimensional computational results as the kink depth increases. The local stress intensity factor solutions of the kinked cracks of finite depths are also presented in terms of those for vanishing kink depth based on the global stress intensity factor solutions and the analytical kinked crack solutions for vanishing kink depth.

Note that Pan and Sheppard (2003) used the basic forms of the stress intensity factor solutions for surface cracks of Newman and Raju (1981) to fit their local $k_{\mathrm{I}}$ and $k_{\mathrm{II}}$ solutions for several kink depths. The local $k_{\mathrm{I}}$ and $k_{\mathrm{II}}$ solutions approach to 0 based on the fitted equations in Pan and Sheppard (2003) when the kink depth approaches to 0. This is not consistent with the fundamentals of the kinked crack solutions and our computational results and, therefore, the fitted equations should not be used for small kink depths. Note that the bulk of the fatigue life of spot welds under lap-shear loading conditions is due to stage I crack growth with small kink depths (Swellam et al., 1992). Therefore, accurate local stress intensity factor solutions are needed for small and finite kinked depths. In contrast to the approach taken by Pan and Sheppard (2003), the local stress intensity factor solutions for kinked cracks of finite depths are expressed in terms of those for vanishing kink depth based on the global stress intensity factor solutions and the analytical kinked crack solutions for vanishing kink depth. The local $k_{\mathrm{I}}$ and $k_{\mathrm{II}}$ solutions appear to be well characterized by the local stress intensity factor solutions for vanishing kink depth as shown in Figs. 13 and

14. Note that the general solutions of the local $k_I$, $k_{II}$ and $k_{III}$ solutions should have the forms as indicated in Eq. (4). A systematic investigation is needed to obtain the local $k_I$, $k_{II}$ and $k_{III}$ solutions along the kinked crack front as functions of $\theta$, $d/t$, $d/c$, $c/b$, $t$, $b$, $t/b$, $W/b$, $V/b$ and $L/b$. However, the computational cost would be significant and prohibitively high.

The fatigue crack growth models proposed by Newman and Dowling (1998) and Lin and Pan (2004) are based on the assumptions that the local stress intensity factor solutions are nearly constant for kinked crack growth through the sheet thickness and the local stress intensity factor solutions are based on the global stress intensity factor solutions and the analytical kinked crack solutions in Cotterell and Rice (1980) for vanishing kink depth. For lap-shear specimens, the assumption of the constant local stress intensity factor solutions seems reasonable based on the three-dimensional finite element computational results obtained in this investigation and the computational results of Pan and Sheppard (2003) that we presented in terms of the kinked crack solutions for vanishing kink depth.

In Lin et al. (in press), the predictions of fatigue lives for lap-shear specimens of dual phase steel based on the fatigue crack growth model are slightly lower than the experimental results. The selection of the material constants for the Paris law is based on those for martensitic steels by consideration of the welding process. If the local stress intensity factor solutions for kinked cracks based on our three-dimensional finite element computations are to be used to predict the fatigue lives of spot welds in lap-shear specimens, the fatigue lives will be substantially lower than the experimental results. Unfortunately, the material constants for the Paris law for the material along the kinked crack paths near the dual phase spot welds are not available. But based on the fatigue crack growth model with consideration of higher local stress intensity factor solutions, the selection of the material constants should be made different in the fatigue crack growth model in Lin and Pan (2004) in order to match with the experimental results. Further investigations of kinked crack growth mechanisms and the fatigue crack growth resistance are needed for this case. Finally, the stress intensity factor solutions for kinked cracks with finite kink lengths are needed for accurate prediction of fatigue lives of spot welds. The stress intensity factor solutions for different normalized kink lengths presented in this paper have been adopted to predict the fatigue lives of aluminum spot friction welds in Lin et al. (2005). Further applications of the stress intensity factor solutions for kinked cracks with finite crack lengths are anticipated.

## Acknowledgments

Partial support of this work from a Ford/Army IMPACT project and a Ford University Research Program is greatly appreciated. Helpful discussions with S.-H. Lin and P.-C. Lin of University of Michigan are greatly appreciated.

## References

Bilby, B.A., Cardew, G.E., 1978. Stress intensity factors at the tips of kinked and forked cracks. The Fourth International Conference on Fracture, University of Waterloo, Ontario, June 19–24, 1977, vol. 3A. Pergamon Press, New York, NY, pp. 197–200.

Cotterell, B., Rice, J.R., 1980. Slightly curved or kinked cracks. International Journal of Fracture 16, 155–169.

Deng, X., Chen, W., Shi, G., 2000. Three-dimensional finite element analysis of the mechanical behavior of spot welds. Finite Elements in Analysis and Design 35, 17–39.

Hibbitt, H.D., Karlsson, B.I., Sorensen, E.P., 2001. ABAQUS User Manual. Version 6-2.

Kitagawa, H., Yuuki, R., Ohira, T., 1975. Crack-morphological aspects in fracture mechanics. Engineering Fracture Mechanics 7, 515–529.

Lin, S.-H., Pan, J., 2004. Fatigue life prediction for spot welds in coach-peel and lap-shear specimens with consideration of kinked crack behavior. International Journal of Materials and Product Technology 20, 31–50.

Lin, S.-H., Pan, J., Wung, P., Chiang, J., in press. A fatigue crack growth model for spot welds in various types of specimens under cyclic loading conditions. To appear in International Journal of Fatigue.

Lin, P.-C., Wang, D.-A., Pan, J., to be submitted for publication. Mode I stress intensity factor solutions for spot welds in lap-shear specimens.

Lin, P.-C., Pan, J., Pan T., 2005. Investigation of fatigue lives of spot friction welds in lap-shear specimens aluminum 6111-T4 sheets based on fracture mechanics. SAE Technical Paper No. 2005-01-1250, Society of Automotive Engineers, Warrendale, PA.

Lo, K.K., 1978. Analysis of branched cracks. Journal of Applied Mechanics 45, 797–802.

Newman, J.A., Dowling, N.E., 1998. A crack growth approach to life prediction of spot-welded lap joints. Fatigue and Fracture of Engineering Materials and Structures 21, 1123–1132.

Newman, J.C., Raju, I.S., 1981. An empirical stress-intensity factor equation for the surface crack. Engineering Fracture mechanics 15, 185–192.

Pan, N., Sheppard, S.D., 2002. Spot welds fatigue life prediction with cyclic strain range. International Journal of Fatigue 24, 519–528.

Pan, N., Sheppard, S.D., 2003. Stress intensity factors in spot welds. Engineering Fracture Mechanics 70, 671–684.

Pook, L.P., 1975. Fracture mechanics analysis of the fatigue behaviour of spot welds. International Journal of Fracture 11, 173–176.

Pook, L.P., 1979. Approximate stress intensity factors obtained from simple plate bending theory. Engineering Fracture Mechanics 12, 505–522.

Radaj, D., Zhang, S., 1991a. Stress intensity factors for spot welds between plates of unequal thickness. Engineering Fracture Mechanics 39, 391–413.

Radaj, D., Zhang, S., 1991b. Simplified formulae for stress intensity factors of spot welds. Engineering Fracture Mechanics 40, 233–236.

Radaj, D., Zhang, S., 1992. Stress intensity factors for spot welds between plates of dissimilar materials. Engineering Fracture Mechanics 42, 407–426.

Radaj, D., Zhaoyun, Z., Mohrmann, W., 1990. Local stress parameters at the weld spot of various specimens. Engineering Fracture Mechanics 37, 933–951.

Satoh, T., Abe., H., Nishikawa, K., Morita, M., 1991. On three-dimensional elastic-plastic stress analysis of spot-welded joint under tensile shear load. Transactions of the Japan welding society 22, 46–51.

Scafe, A., Joaquin, A., 2004. Friction stir welding of extruded aluminum for automotive applications. SAE Technical Paper 2004-01-1333, Society of Automotive Engineers, Warrendale, Pennsylvania.

Shih, C.F., Asaro, R.J., 1988. Elastic-Plastic Analysis of Cracks on Bimaterial Interfaces: Part I—small scale yielding. Journal of Applied Mechanics 55, 299–316.

Swellam, M.H., Kurath, P, Lawrence, F.V., 1992. Electric-potential-drop studies of fatigue crack development in tensile-shear spot welds. In: Mitchell, M.R., Landgraf, R.W. (Eds.), Advances in Fatigue Lifetime Predictive Techniques. ASTM STP 1122. American Society for Testing and Materials, Philadelphia, pp. 383–401.

Swellam, M.H., Banas, G., Lawrence, F.V., 1994. A fatigue design parameter for spot welds. Fatigue and Fracture of Engineering Materials and Structures 17, 1197–1204.

Wang, D.-A., Lin, S.-H., Pan, J., 2005. Stress intensity factors for spot welds and associated kinked cracks in cup specimens. International Journal of Fatigue 27, 581–598.

Wang, D.-A., Lin, P.-C., Pan, J., in press. Geometric functions of stress intensity factor solutions for spot welds in lap-shear specimens. International Journal of Solids and Structures, doi:10.1016/j.ijsolstr.2005.05.037.

Wung, P., Stewart, W., 2001. Method of analyzing spot welded structures. Patent No. US 6,186,011 B1.

Zhang, S., 1997. Stress intensities at spot welds. International Journal of Fracture 88, 167–185.

Zhang, S., 1999. Approximate stress intensity factors and notch stresses for common spot-welded specimens. Welding Journal 78, 173s–179s.

Zhang, S., 2001. Fracture mechanics solutions to spot welds. International Journal of Fracture 112, 247–274.